Arranz, G.; Moriche, M.; Uhlmann, M.; Flores, O.; García-Villalba, M. (2018). Kinematics and dynamics of the auto-rotation of a model winged seed. *Bioinspiration & Biomimetics*, 13(3): 036011.

DOI: https://doi.org/10.1088/1748-3190/aab144

Kinematics and dynamics of the auto-rotation of a model winged seed

G Arranz[1], M Moriche[1], M Uhlmann[2], O Flores[1] & M García-Villalba[1]
[1] Universidad Carlos III de Madrid, Spain
[2] Karlsruhe Institute of Technology, Germany

Abstract

Numerical simulations of the auto-rotation of a model winged seed are presented. The calculations are performed by solving simultaneously the Navier-Stokes equations for the flow surrounding the seed and the rigid-body equations for the motion of the seed. The Reynolds number based on the descent speed and a characteristic chord length is varied in the range $80 - 240$. Within this range, the seed attains an asymptotic state with finite amplitude auto-rotation, while for smaller values of the Reynolds number no auto-rotation is observed. The motion of the seed is characterized by the coning and pitch angles, the angular velocity and the horizontal translation of the seed. The values obtained for these quantities are qualitatively similar to those reported in the literature in experiments with real winged seeds. When increasing the Reynolds number, the seed tends to rotate at higher speeds, with less inclination with respect to the horizontal plane, and with a larger translation velocity. With respect to the aerodynamic forces, it is observed that, with increasing Reynolds number, the horizontal components decrease in magnitude while the vertical component increases. The force distribution along the wing span is characterized using both global and local characteristic speeds and chord lengths for the non-dimensionalisation of the force coefficients. It is found that the vertical component does not depend on the Reynolds number when using local scaling, while the chordwise component of the force does.

Keywords: Winged seed, auto-rotation, numerical simulation.

1 Introduction

Nature has shown to be an excellent engineer. Therefore, it is not surprising that several tree species are able to take advantage of wind and turbulent gusts to disperse their seeds thanks to their suitable shapes. More surprising is the fact that this dispersal can range from tens of meters to kilometers (Nathan, 2006). Some of these seeds, often called straying seeds, rely on their small weight to surface ratio to perform a parachuting flight thanks to the drag force acting on them (Burrows, 1975; Minami and Azuma, 2003). However, there are other kind of seeds which are able to create lifting forces opposite to gravity to reduce their descent speed and increase their dispersal distance under lateral winds. This type of seeds, usually known as winged seeds, or *samaras*, generate these aerodynamic forces executing auto-rotational flight as they fall (Azuma, 1992, chapter 6). Thus, samaras have much larger wing loading (weight to exposed surface ratio) than straying seeds (Minami and Azuma, 2003).

Winged seeds from different species have different size and shape, but all of them exhibit a similar physical structure: a thin, leaf-like wing with a thicker leading edge; and a nut (or embryo) at one side of the wing. These seeds have received a lot of attention from the scientific community during the last decades (Norberg, 1973; Green, 1980; Azuma and Yasuda, 1989; Rosen and Seter, 1991; Seter and Rosen, 1992a; Yasuda and Azuma, 1997). The reasons for this attention are mainly two. First, the reduction of the descent speed in auto-rotation compared to the free falling velocity, which has obvious engineering applications. Second, winged seeds have high auto-rotation stability, meaning that they are able to sustain auto-rotation when they encounter wind disturbances (Lee and Choi, 2017), and when their shape is drastically changed (Varshney *et al.*, 2012). The gist of this stable auto-rotation is a subtle coupling between seed's inertia and aerodynamic forces (Varshney *et al.*, 2012). In this fashion, samaras possess self-stability governed just by their structural pattern, without the need of any active actuator, like neuromuscular control in animal flight (Norberg, 1973).

These natural abilities have fostered the development of aerial vehicles based on samaras. Examples of these are the *Samarai* developed by Lockheed-Martin (Obradovic *et al.*, 2012; Fregene and Bolden, 2010) and the robotic samara developed by Ulrich *et al.* (2010), which have a propeller installed to be remotely controlled. Similarly, Pounds and Singh (2015) present a sensor based on the shape of a winged seed to exploit the dispersal capabilities of these seeds. In this fashion, several of these sensors are deployed from an aerial vehicle with the scope of monitoring a target area.

However, the design of efficient vehicles entails a more detailed comprehension of the auto-rotation phenomena, which is difficult to study. The coupling between the seed's inertia and aerodynamic forces poses several difficulties in order to analyse the problem from a theoretical perspective. The descent speed, angular velocity, and attitude of the seed as it auto-rotates will be largely defined by the aerodynamic forces, which in turn will vary depending on the former parameters. Hence, a theoretical approach of the problem entails, ineluctably, a model of the aerodynamic forces based on seed's kinematics. The vast majority of these models are simplified models based on the *blade element theory*, which do not consider the existence of a leading edge vortex (LEV), or three dimensional effects of the flow, among others (Azuma and Yasuda, 1989; Seter and Rosen, 1992b).

On the other extreme, thanks to advances in flow visualization techniques such as digital particle image velocimetry (DPIV), it is possible to measure the velocity field around an actual samara in auto-rotation. In fact, this technique allowed Lentink *et al.* (2009) to visualize a stable LEV created on the upper surface of winged seeds as they auto-rotate. Nonetheless, although DPIV allows to study the flow field, the force distribution is not easily measured experimentally. Consequently, force distributions are usually extrapolated from the velocity field as in Lentink *et al.* (2009), Salcedo *et al.* (2013) and Limacher and Rival (2015).

These difficulties can be overcome with the use of Direct Numerical Simulations (DNS) with a 2-way coupling between the fluid and the solid dynamics, where the aerodynamic forces are directly obtained and hence do not need to be modelled (Uhlmann, 2005). Moreover, systematic variations of a single parameter of the problem (e.g., seed's inertia, density ratio or Reynolds number) are easily performed using DNS, allowing to study the isolated effect of these parameters on the auto-rotation of the seed.

In the present study we take advantage of this latter approach, and perform DNS of the auto-rotation of a winged-seed at different Reynolds numbers, $Re = w_d c/\nu$ (where w_d is the descent speed, c is the characteristic chord of the seed's wing, and ν is the dynamic viscosity of air). The objective is to investigate auto-rotation at lower Reynolds number than typical values found in nature (which are of the order of $Re \sim 700$), studying the change of the kinematics and the aerodynamic forces with Re while keeping the seed's geometry and inertia constant. The analysis focuses on the motion and attitude of the model winged seed, and on the resulting aerodynamic forces. The analysis of the flow surrounding the seed is reported elsewhere (Arranz *et al.*, 2018). The structure of the paper is as follows. Section 2 presents the methodology used for the simulations, including the numerical methods, geometric and inertial model of the seed, etc. The results of the simulations are presented and discussed in section 3 in terms of the seed kinematics and the distribution of aerodynamic forces. Finally, the conclusions are presented in section 4.

2 Methodology

2.1 Numerical model

The problem under study is the motion of a winged seed immersed in ambient fluid. Four different reference frames are used in the present analysis: Σ_L, Σ_p, Σ_c and Σ_R. Σ_L is the laboratory reference frame: an inertial reference frame with axes x_L, y_L and z_L, the latter pointing upwards. Σ_p is a body-fixed reference frame centered at the seed's gravity centre, G, whose axes coincide with the principal axes of inertia of the seed. Both Σ_L and Σ_p are sketched in figure 1a, and are used to solve the equations of motion of the seed, as discussed in the next paragraph. The other two reference frames sketched in figure 1b, Σ_c and Σ_R, are defined in terms of the seed's geometry and are used for analysing and visualizing purposes. Σ_c is a body fixed reference frame centered at the centre of the nut; with z_c normal to the wing of the seed and y_c pointing towards the tip of the wing. On the other hand Σ_R is a non-inertial reference frame whose attitude is defined by its axes z_R, parallel to z_L, and y_R, which is the projection of y_c on the horizontal plane ($z_L = 0$).

We define $\mathbf{i}$, $\mathbf{j}$ and $\mathbf{k}$ to be the unit vectors in the x, y and z directions, respectively. The subscript of these vectors indicate the reference frame they belong to, e.g.: $\mathbf{i}_L$ is the unit vector of x_L. On the other hand, to specifically indicate that a vector is expressed in a certain basis, the superscript notation, $\mathbf{x}^Y$,

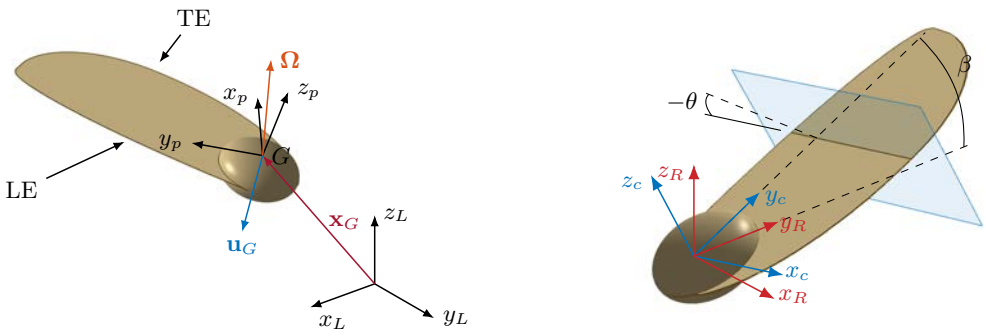

Figure 1: (a) Sketch of Σ_L and Σ_p. The position vector of the gravity centre, $\mathbf{x}_G$, the velocity vector of G, $\mathbf{u}_G$, and the angular velocity vector, $\boldsymbol{\Omega}$, are also displayed. LE and TE stands for the leading edge and the trailing edge of the wing seed, respectively. (b) Sketch of Σ_c and Σ_R. The two angles that define the attitude of the seed, the coning angle, β, and the pitch angle, θ, are also displayed.

is used, where Σ_Y is the basis. Therefore, $\mathbf{x}^Y$ indicates that the components of $\mathbf{x}^Y$, namely, (x_1, x_2, x_3) are $x_1 = \mathbf{x} \cdot \mathbf{i}_Y$, $x_2 = \mathbf{x} \cdot \mathbf{j}_Y$ and $x_3 = \mathbf{x} \cdot \mathbf{k}_Y$.

The equations that govern the motion of the seed are:

$$m_s \dot{\mathbf{u}}_G = \mathbf{F}_{ext}, \tag{1}$$

$$\overline{\overline{I}}_G \dot{\boldsymbol{\Omega}} + \boldsymbol{\Omega} \times \overline{\overline{I}}_G \boldsymbol{\Omega} = \mathbf{M}_G. \tag{2}$$

In (1) and (2), dot indicates time derivative, m_s is the mass of the seed, $\mathbf{u}_G$ is the absolute velocity of the gravity centre (i.e. with respect to Σ_L), $\mathbf{F}_{ext}$ are the external forces acting upon the seed, $\boldsymbol{\Omega}$ is the angular velocity, $\overline{\overline{I}}_G$ is the tensor of inertia about the gravity centre of the seed and $\mathbf{M}_G$ are the moments about the gravity centre. Note that (2) is expressed in a body-fixed frame of reference. The external forces are the gravity, $-m_s g \mathbf{k}_L$, where g is the gravity acceleration; buoyant force, $m_s \rho_f / \rho_s g \mathbf{k}_L$, where ρ_f and ρ_s are the fluid and seed densities, respectively; and aerodynamic forces, $\mathbf{F}$. On the other hand, we consider that the moment $\mathbf{M}_G$ is only due to the aerodynamic forces, which is strictly true for a samara of uniform density.

Equation (1) is solved in the inertial reference frame Σ_L, whereas (2) is solved in the body reference frame Σ_p. The latter simplifies the resolution of (2) since the tensor $\overline{\overline{I}}_G$, when expressed in Σ_p, is constant and diagonal, with the elements of this diagonal corresponding to the principal moments of inertia of the seed.

In order to solve (1) and (2), the attitude of Σ_p with respect Σ_L must be known. This is done here with the quaternion formulation, which avoids the possible singularities that may arise with the Euler angles (see Tewari, 2007). The quaternion, $\mathbf{Q} = (Q_1, Q_2, Q_3, Q_4)$, is defined as:

$$Q_i = e_i \sin\left(\frac{\varphi}{2}\right) \quad (i = 1, 2, 3) \quad \text{and} \tag{3}$$

$$Q_4 = \cos\left(\frac{\varphi}{2}\right), \tag{4}$$

where $\mathbf{e} = (e_1, e_2, e_3)$ is a unit vector along the rotation axis and φ is the angle of rotation. Hence, the quaternion $\mathbf{Q}$ defines a rotation that converts Σ_L into Σ_p. It is possible to show that the time evolution of $\mathbf{Q}$ is:

$$\frac{\mathrm{d}\mathbf{Q}}{\mathrm{d}t} = \frac{1}{2} \overline{\overline{\Omega}} \mathbf{Q}, \tag{5}$$

where $\overline{\overline{\Omega}}$ depends on $\boldsymbol{\Omega}^p = (p, q, r)$ (superscript p indicates that $\boldsymbol{\Omega}$ is expressed in Σ_p), namely:

$$\overline{\overline{\Omega}} = \begin{pmatrix} 0 & r & -q & p \\ -r & 0 & p & q \\ q & -p & 0 & r \\ -p & -q & -r & 0 \end{pmatrix}. \tag{6}$$

For further details about quaternion formulation the reader is referred to Tewari (2007).

(a) (b)

Figure 2: (a) *Tipuana Tipu* seed. (b) Simplified model of *Tipuana Tipu* seed used in the simulations. Top view and side view of the model. C is the geometric centre of the nut, and G is the gravity centre of the seed. For reference Σ_p and Σ_c are also sketched.

The solution to the system of equations (1), (2) and (5) yields the evolution of the seed's dynamics. However, the aerodynamic forces and moments acting on the seed must be known. To compute them, we solve the incompressible Navier-Stokes equations,

$$\nabla \cdot \mathbf{u} = 0, \tag{7a}$$

$$\frac{\partial \mathbf{u}}{\partial t} + (\mathbf{u} \cdot \nabla)\mathbf{u} = -\frac{1}{\rho_f}\nabla p_f + \nu \nabla^2 \mathbf{u}, \tag{7b}$$

where $\mathbf{u}$ is the fluid velocity, p_f is the pressure and ν is the kinematic viscosity of the fluid. Equations (7a) and (7b) are solved in the inertial reference frame, Σ_L.

Direct numerical simulations are carried out to solve (7a) and (7b) with TUCAN: an in-house solver of the Navier-Stokes equations that uses a fractional step method and centered, second-order finite differences for spatial derivatives in a staggered grid; time evolution is performed by a semi-implicit three stages Runge-Kutta method; and the presence of the body inside the fluid is modelled by means of an Immersed Boundary Method (IBM) (Uhlmann, 2005). The code is described in Moriche (2017) and it has been extensively validated and applied to aerodynamic flows (Moriche *et al.*, 2016, 2017).

The coupling between the equations of motion and the Navier-Stokes equations is implemented as in Uhlmann (2005). It is a weak coupling, in which at each Runge-Kutta stage, the flow is solved first to obtain $\mathbf{F}$, and then the seed dynamics are updated. The difference with Uhlmann (2005) is that eq. (2) is expressed in the principal axes of inertia, entailing the computation of (5). On the contrary, Uhlmann (2005) modelled spheres which have isotropic inertia properties, so that $\overline{\overline{I}}_G$ is constant regardless of the reference frame, and there is no need to keep track of the orientation of the sphere.

To validate the present algorithm, we have computed the motion of an oblate spheroid of aspect ratio 1.5 and density ratio $\rho_s/\rho_f = 2.14$ settling under gravity in ambient fluid. For this configuration, high-fidelity data from a boundary-conforming spectral-element method is available (Chrust, 2012). Using a grid resolution of 24 points per major axis, we have reproduced the instability regimes described in Chrust (2012), and their transitions with increasing the Galileo number, $Ga = \sqrt{(\rho_s/\rho_f - 1)gV}/\nu$, where V is the volume of the spheroid. Particularly, our validation runs show a steady vertical trajectory for $Ga = 96$, steady oblique for $Ga = 110$, oscillating oblique for $Ga = 122$ and vertical with lateral oscillations for $Ga = 150$.

2.2 Geometric, inertial and aerodynamic model

For the simulations, we use a simplified model based on the *Tipuana Tipu* seed shown in figure 2a. The use of a simplified model instead of replicating the actual shape of a real samara is well justified if one looks at the vast variety of winged-seed's geometries that exist in Nature (Azuma and Yasuda, 1989; Green, 1980). This simplified model consists of a nut, which is modelled as an oblate spheroid, and a wing modelled as a flat plate (see figure 2b).

The shape of the wing consists of four quarters of ellipse which are tangent to each other, following the same approach as Pedersen and Żbikowski (2006) to model insect wings (figure 3a). Note that similarities between winged seeds and animal wings were already reported by Norberg (1973) and have been recently analysed by Ortega-Jiménez *et al.* (2017) in terms of their auto-rotation.

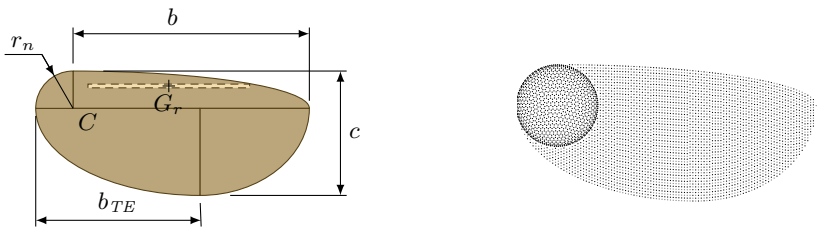

(a) (b)

Figure 3: (a) Sketch of the wing planform together with the fictitious rod and its gravity centre position, G_r. (b) Discretization of the samara seed.

We define the characteristic chord of the wing to be c (see figure 3a). The dimensions of the wing are $b/c = 1.9$, $b_{TE}/c = 1.32$ and $r_n/c = 0.3$, as shown in figure 3a. Note that r_n is the semi-major axis of the nut, whose aspect ratio is 0.6 (i.e. ratio between the semi-minor axis and the semi-major axis of the ellipsoid).

For the inertia model, we assume that the seed has constant density ρ_s, the oblate spheroid is solid, and the wing is a flat plate of thickness $t = 0.005c$. Moreover, the effect of the thick leading edge –which plays a role of the utmost importance in auto-rotation stability (Norberg, 1973; Seter and Rosen, 1992a; Yasuda and Azuma, 1997), is also accounted for with a fictitious rod, shown in figure 3a. The dimensions of this fictitious rod are adjusted so that for the spanwise sections of the wing affected by the rod, the distance from the leading edge to the mass centre is smaller than 30% of $c(y_c)$, in accordance to Norberg (1973). The rod is defined by its radius $r_r = 0.05c$ and length $l_r = 1.54c$, the position of its gravity centre, $\mathbf{CG_r} = -0.25c\mathbf{i}_c + 0.77c\mathbf{j}_c$ (where $\mathbf{CG_r}$ denotes the vector from C to G_r), and the orientation of its longitudinal axis, parallel to y_c (see figure 3a). In this fashion, the resulting inertia tensor of the seed with respect to C expressed in Σ_c, namely, $\overline{\overline{I}}^c_C$, is:

$$\overline{\overline{I}}^c_C = \begin{bmatrix} 19.26 & -0.99 & 0 \\ -0.99 & 3.20 & 0 \\ 0 & 0 & 21.57 \end{bmatrix} \cdot 10^{-3}\rho_s c^5,$$

and the gravity centre of the seed with respect to Σ_c turns out to be, $\mathbf{CG} = -0.018c\mathbf{i}_c + 0.185c\mathbf{j}_c$. The principal tensor of inertia turns out to be:

$$\overline{\overline{I}}^p_G = \begin{bmatrix} 16.29 & 0 & 0 \\ 0 & 3.17 & 0 \\ 0 & 0 & 18.56 \end{bmatrix} \cdot 10^{-3}\rho_s c^5.$$

2.3 Computational set-up

To perform the simulations, the seed is placed in a cubic fluid domain of side $10.66c$. Periodic boundary conditions are imposed at the lateral boundaries, whereas a uniform inflow is imposed at the bottom boundary ($z^L = -3.66c$), and an advective boundary condition is imposed at the top boundary. The computational domain is discretized with a uniform Cartesian grid of 512^3 points, which corresponds to 48 grid points per length c. This resolution has been set after performing a grid refinement study, presented in Appendix A. Likewise, the seed is also discretized into points (see figure 3b) whose resolution is based on the requirements of the immersed boundary method (Uhlmann, 2005). Particularly, the seed consists of 5674 points. Since the wing thickness t is much smaller than the grid spacing, $\Delta = c/48$, the wing is modelled as a flat surface. The time step, Δt, has been selected so that $CFL = u_{max}\Delta t/\Delta \leq 0.2$, where u_{max} is the maximum velocity in the flow field.

The seed is free to rotate and its gravity centre can move on an horizontal plane, but we restrain its motion in the vertical direction. Note that fixing $z^L_G = 0$ (and $w^L_G = \dot{w}^L_G = 0$) and imposing a constant inflow velocity w_d results in a configuration that is analogous to the *natural* configuration: a seed descending at a constant speed w_d in a fluid at rest. The advantage of this procedure is that it allows a finer control of the simulation parameters (note that in the *natural* configuration the descent velocity of the seed, w_d, is unknown), and a simpler set-up of the computational domain: in the *natural* configuration, when the inflow velocity is not exactly equal to w_d, the seed is eventually advected outside of the computational domain.

Finally, it should be noted that fixing the vertical position of the gravity centre of the seed means that the the vertical component of (1) is not solved, which is the only equation involving the gravity acceleration, g. Indeed, once the seed has reached a stable auto-rotative state, we can use the value of F_z^L obtained in the simulation to estimate the value of g required to have a equilibrium of forces in the vertical direction,

$$g = \frac{F_z^L}{m_s}\frac{\varrho}{\varrho - 1}, \tag{8}$$

where F_z^L is the vertical component of $\mathbf{F}^L$, and $\varrho = \rho_s/\rho_f$ is the density ratio. Then, the simulation can be restarted in the *natural* configuration (i.e., solving all components of (1) and allowing the seed to move freely in the domain) using the value of g computed in (8). This approach is proposed by Uhlmann and Dušek (2014). We followed this procedure for a single case, obtaining a dynamical response of the samara in the *natural* configuration virtually indistinguishable to the results reported in section 3.

When fixing $z_G^L = 0$, the problem depends on two non-dimensional numbers, the density ratio, ϱ, and the Reynolds number, Re. In our simulations $\varrho = 300$ (which is a reasonable value close to reality) and we vary the Reynolds number, $Re = [80, 160, 240]$. Note that these Re are on the lower limit of typical Reynolds number of actual winged-seeds, which ranges from $Re \simeq 350$ to 1540 (Green, 1980; Azuma and Yasuda, 1989; Salcedo *et al.*, 2013).

To trigger the auto-rotation of the seed, the simulations are started with initial conditions: $\mathbf{\Omega}_0 = \Omega_0 \mathbf{k}_L = c/w_d \mathbf{k}_L$, $\mathbf{u}_G = 0$, and z_p parallel to z_L, which is equivalent to an initial rotation about G. To check the effect of the value Ω_0 on the final auto-rotative steady state, we also started a simulation with $\Omega_0 = \frac{1}{2}c/w_d$, yielding the same auto-rotative state. It should be highlighted that in both cases, the initial angular velocity is lower than the final angular velocity.

The previous procedure is followed to start the simulation with $Re = 240$ and with a lower resolution, $256 \times 256 \times 256$ grid points, to save computational time. Once the seed has performed several cycles, at a given time t_1, the flow field is interpolated into a finer grid of $512 \times 512 \times 512$ grid points and the simulation is restarted with this denser mesh. For $Re = 80$ and 160, we use the flow field and the seed attitude at t_1 to restart the simulation with the desired Re at the reduced resolution. After the seed has performed several cycles with the new Reynolds number, the field is interpolated into the finer mesh, as explained previously, and the simulations are continued.

3 Results

For all cases under study the seed attained an asymptotic state with finite amplitude auto-rotation. We performed additional simulations at $Re \leq 80$. First, the simulation was started directly at $Re = 80$ with the initial condition described in section 2.3. In this case the seed failed to auto-rotate, suggesting that the problem presents hysteresis. Likewise, starting with the auto-rotating simulation at $Re = 80$, we successively decreased the Reynolds number and it was observed that there may be a lower limit $Re \approx 50$ below which auto-rotation is no longer possible. Nevertheless, the aim of this study is not to determine what is the exact Reynolds number at which auto-rotation is no longer possible so that additional simulations should be performed in the future in order to establish this value accurately.

For a visualization of the simulations, figure 4 shows the trajectory and orientation of the seed at $Re = 240$ descending at a constant speed w_d. The seed is depicted at equispaced time instants. In addition, the trajectory of the wing tip and G are also displayed.

Although in figure 4 only $Re = 240$ is shown, the motion is qualitatively similar for all Re under study. From figure 4, one can infer that the seed spins about a vertical axis; thus, $\mathbf{\Omega}$ is parallel to $\mathbf{k}_L$ (except for small deviations which never exceed 2°). As a result, the wing tip describes a helical path. On the contrary, G follows almost a vertical path (with small displacements in x_L and y_L), suggesting that the rotation axis is very close to G.

As mentioned in section 1, auto-rotation is due to a tight coupling between the aerodynamic forces and the seed's motion. In turn, aerodynamic forces are greatly dependent on flow structures, which are represented in figure 5. This figure displays iso-surfaces of the second invariant of the velocity gradient tensor, Q, for the case with $Re = 240$ (i.e. the Q-criterion of Hunt *et al.*, 1988 for the identification of vortical structures). Three main vortical structures can be identified: the wing tip vortex; the wake shed by the nut; and the LEV (i.e, leading edge vortex) which is formed above the wing and corresponds to the darker blue surface in figure 5. As a consequence of the rotation, the wing tip vortex wraps about a vertical axis, forming a helical structure, similar to the trajectory of the wing tip shown in figure 4. The

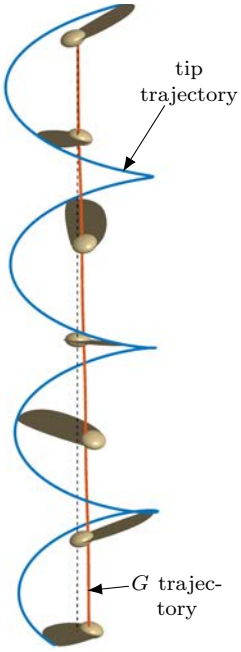

Figure 4: Three dimensional view of the seed's trajectory for $Re = 240$. (——) Trajectory of the wing's tip, (——) Trajectory of the gravity centre. The attitude of the seed is depicted at different equidistant time instants. The dotted line is a vertical axis parallel to $\mathbf{k}_L$.

vortex shed by the nut has also a helical shape, but with a smaller radius. A more detailed analysis of the corresponding flow fields is reported in Arranz *et al.* (2018).

Figure 4 shows that the seed reaches a quasi-stationary state. Consequently, in the following sections we will discuss time averaged quantities over the last 4 periods of the simulations. These averaged quantities are denoted with angular brackets, e.g.: $\langle x \rangle$. Likewise, non-dimensional variables are denoted as $\tilde{x}$.

3.1 Seed kinematics

Quantitatively, the effect of the Reynolds number on the motion of the seed is assessed by the change of the coning angle, β, and the pitch angle, θ, the angular velocity, $\mathbf{\Omega}$, and the displacement of G. β is the angle between $\mathbf{j}_c$ and the horizontal plane, and it gives an indication of how tilted the winged seed is with respect to the horizontal plane. On the other hand, θ is the angle between $\mathbf{i}_c$ and $\mathbf{i}_R$ and it can be seen as a geometric angle of attack. The definitions of both β and θ are depicted in figure 1b. Mathematically, β and θ are defined as:

$$\beta = \cos^{-1}\left(\mathbf{j}_c \cdot \mathbf{j}_R\right) \tag{9}$$

$$\theta = -\mathrm{sgn}(\mathbf{i}_c \cdot \mathbf{k}_L)\cos^{-1}\left(\mathbf{i}_c \cdot \mathbf{i}_R\right) \tag{10}$$

Figure 6 displays the average of the modulus of the non-dimensional angular velocity (namely, $\tilde{\Omega} = \Omega c/w_d$) as a function of Re, together with its standard deviation. In figure 6 one can appreciate that the standard deviation for all the cases is very small, indicating that $\tilde{\Omega}$ is indeed rather constant. Looking at the evolution of $\langle\tilde{\Omega}\rangle$ with Re, one can observe that it increases with Re, i.e. the seed spins faster as the Reynolds number increases. The values of $\langle\tilde{\Omega}\rangle$ are also gathered in table 1.

Figure 7 shows the temporal evolution of β and θ for the different Reynolds numbers. The time $t = 0$ corresponds to the time when the simulations are started on the fine grid. Regardless of Re, both angles show an oscillatory behaviour about a mean value after an initial transient. The initial variation is caused by the change of the resolution, as explained in section 2.3. Nonetheless, the oscillation of both angles is small, not exceeding 2°. Note that there is a phase shift of approximately $\pi/2$ between β and θ. Also, the oscillations observed in figure 7 have a fixed frequency. This frequency is equal to $\Omega/2\pi$ for all Reynolds numbers, meaning that the period of the oscillations is the period of the rotation. It is interesting to recall that this oscillatory behaviour has also been observed experimentally (Ulrich and Pines, 2012). This issue will be discussed further below.

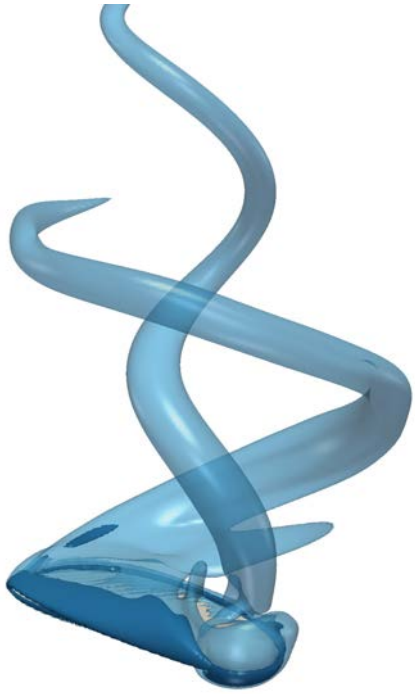

Figure 5: Iso-surfaces of the Q-criterion for $Re = 240$. Light blue iso-surface $\tilde{Q} = 0.5$, dark blue iso-surface $\tilde{Q} = 5$, where $\tilde{Q} = Qc^2/w_d^2$.

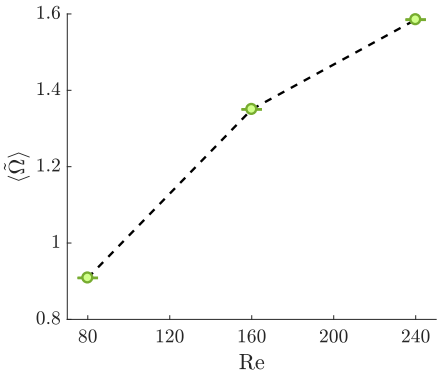

Figure 6: Evolution of $\tilde{\Omega}$ averaged over the last four periods, $\langle\tilde{\Omega}\rangle$, as a function of Re. The standard deviation is depicted with error bars.

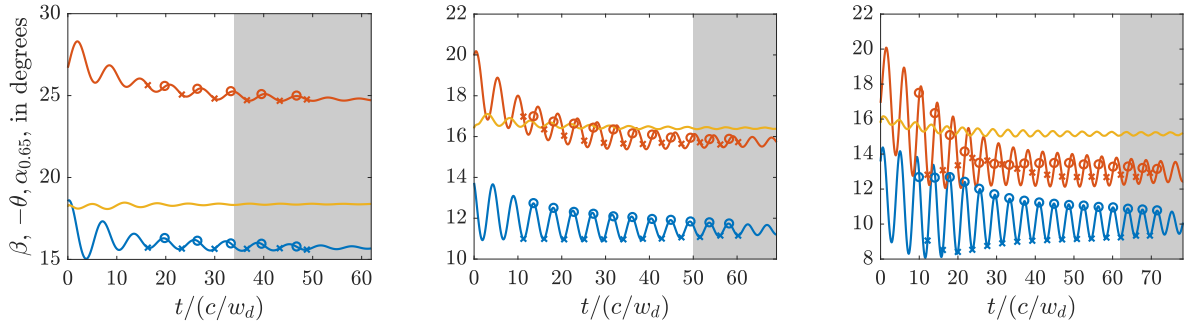

(a) $Re = 80$ (b) $Re = 160$ (c) $Re = 240$

Figure 7: Temporal evolution of β (—); θ (—); and the angle of attack at $0.65b$, $\alpha(y_c = 0.65b)$ (—). Symbol (×) corresponds to the time instant when fluid relative velocity is local maximum; (○) are the time instants when fluid relative velocity is local minimum. The shaded region correspond to the last four periods, where the averages are calculated.

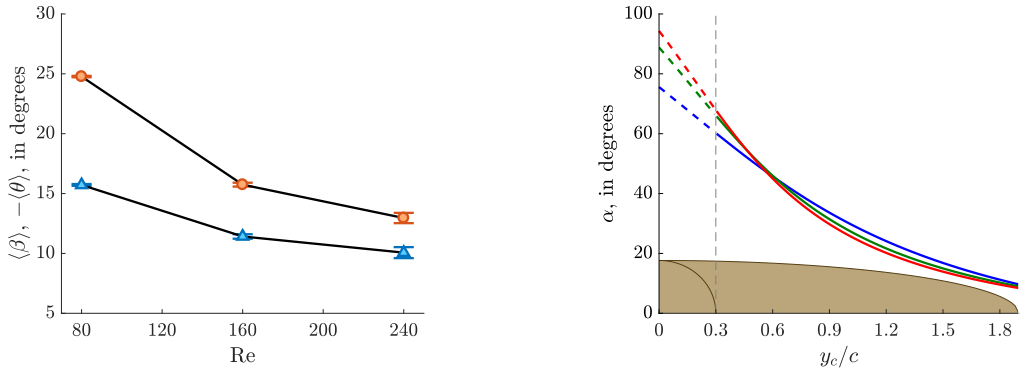

(a) (b)

Figure 8: (a) Evolution of $\langle\beta\rangle$ (▲), and $-\langle\theta\rangle$ (●) as a function of Re. The standard deviation of β and $-\theta$ is depicted with error bars. (b) Angle of attack distribution along the span of the seed's wing. (——) $Re = 80$, (——) $Re = 160$ and (——) $Re = 240$. The dashed vertical line depicts the start of the nut.

	Species	Re	$\widehat{Re}$	$\langle\tilde{\Omega}\rangle$	$\langle\beta\rangle$	$-\langle\theta\rangle$	$\langle\tilde{r}_{GR}\rangle$	λ
Present simulations	–	80	63	0.91	15.72	24.77	$2.7 \cdot 10^{-2}$	1.66
	–	160	126	1.35	11.49	15.82	$1.2 \cdot 10^{-2}$	2.52
	–	240	188	1.58	10.06	13.06	$0.8 \cdot 10^{-2}$	2.96
Green (1980)	*Acer rublum*	–	723	–	36.3	12.5	–	2.89
	Acer saccharum	–	1673	–	12.9	9.0	–	3.32
	Acer saccharinum	–	1880	–	27.3	10.6	–	4.28
Azuma and Yasuda (1989)	*Acer palmatum Thunb*	–	276	–	15.0	0.90	–	2.04
	Acer palmatum Thunb. var	–	457	–	27.6	1.39	–	2.27
	Acer diabolicum Blume	–	459	–	23.7	1.17	–	3.57
Salcedo *et al.* (2013)	*Swietenia macrophylla*	–	1670	–	20.2	–	–	2.21

Table 1: Average values of the kinematics ($\langle\tilde{\Omega}\rangle$, $\langle\beta\rangle$, $\langle\theta\rangle$, $\langle\tilde{r}_{GR}\rangle$ and λ) as function of Re. $\langle\beta\rangle$ and $\langle\theta\rangle$ are given in degrees. For comparison, the table gathers experimental values from the existing literature for different species.

Figure 8a shows the evolution of the mean coning angle, $\langle\beta\rangle$, and the mean pitch angle, $\langle\theta\rangle$, with the Reynolds number. The angles are averaged over the last 4 periods (shaded region in figure 7), and their standard deviation is also depicted in the plot by means of vertical bars. One should recall that θ is always negative, and that is why both figure 7 and figure 8a show $-\theta$. A negative pitch angle means that if the axis y_c would lie on the horizontal plane, the leading edge of the seed would be below this horizontal plane. As the Reynolds number is increased both the coning and the pitch angle decrease (in absolute magnitude). Thus, the wing of the seed tends to be more parallel to the horizontal plane as Re is increased. Note that the growth of the standard deviation with Re means that the amplitude of the oscillations increases, a fact that one can appreciate in figure 7. The values of $\langle\beta\rangle$ and $\langle\theta\rangle$ are also gathered in table 1.

We now proceed to compare our results with the kinematics of actual seeds. To do so, table 1 shows experimental values of the coning angle, the pitch angle and the tip speed ratio, λ, found in the literature. Since in all the references the Reynolds number is based on the mean chord, $\hat{c} = S/b_w$, where S is the total surface of the wing and b_w is the total span of the wing ($b_w = b + r_n$ in our case), we define a new Reynolds number for the comparison, $\widehat{Re} = w_d\hat{c}/\nu$. It should be noted that the seeds reported in table 1 belong to different species, having different geometries and inertias. This precludes a quantitative comparison with our results. For the same reason, an analysis of the effect of the Re on the kinematics of the seeds cannot be assessed with the experimental values of table 1. This analysis has to rely only on the present simulation data.

Despite the simplifications of our model (flat wing, no surface roughness, imposed inertia tensor), the kinematics of the seed are qualitatively similar to experiments found in existing literature. The coning angle of the different seeds ranges between 12° and 36°. Nonetheless, table 1 shows that within our simulations $\langle\beta\rangle$ agrees with the lower limit of the coning angle measured in experiments. However, the trend exhibited in figure 8a is a decrease of $\langle\beta\rangle$ with the Reynolds number. If this tendency is followed, lower $\langle\beta\rangle$ would be expected for higher Re, in disagreement with experiments. This discrepancy could be attributed to the simplifications of the model. However, the behaviour of this trend might change for higher Re.

Comparison of the pitch angle is more cumbersome due to the difficulty in measuring it experimentally. Moreover, there is no consensus of the definition of θ. For instance, Green (1980) defines θ as "tilt of wing in plane of rotation", whereas Azuma and Yasuda (1989) defines θ at a given spanwise section. Therefore, we limit the comparison to the sign of $\langle\theta\rangle$, which is always negative in both the experiments and in our results.

In order to compare the angular velocity, the tip speed ratio, λ, is used (Miller *et al.*, 1997). This parameter is computed as the ratio between the tip speed due to angular velocity (roughly $b\langle\tilde{\Omega}\rangle\cos\langle\beta\rangle$) and the descent speed, w_d. The tip speed ratio is gathered in table 1. In the literature, λ ranges from approximately 2 to 3.3. The values of the simulations are within the experimental range (except the case $Re = 80$, which is slightly lower).

The combined effect of β, θ and $\mathbf{\Omega}$ determines the angle of attack, $\alpha(y_c)$, which is an important quantity in aerodynamics. Mathematically, α can be expressed as

$$\alpha(y_c) = \tan^{-1}\left(\frac{\mathbf{u}_e(y_c)\cdot\mathbf{k}_c}{\mathbf{u}_e(y_c)\cdot\mathbf{i}_c}\right), \tag{11}$$

where $\mathbf{u}_e(y_c) = w_d\mathbf{k}_L - \mathbf{u}_G - \mathbf{\Omega}\times(y_c\mathbf{j}_c)$ is the effective velocity at each spanwise section. Figure 8b depicts the angle of attack distribution along the span for the different Re. It is found that the angle of attack distribution is very similar for the three Re, specially for $y_c > 0.6c$. For the outer spanwise positions, the local angle of attack slightly decreases with the Reynolds number. The temporal evolution of α is similar to β and θ, namely, it oscillates with a frequency of $\Omega/2\pi$. However, the amplitude of the oscillations is one order of magnitude smaller than those of β and θ, although they also increase with Re. This phenomenon is illustrated in figure 7, where the temporal evolution of α at $y_c = 0.65b$ is depicted. The selection of this particular spanwise section is somewhat arbitrary, but similar plots are obtained for other sections (specially in terms of the effect of the Reynolds numbers).

We turn now our attention to the motion of G in the horizontal plane. Recall that, as discussed in figure 4, the velocity of G in the horizontal plane is not zero. Indeed figure 9a shows the trajectory of the gravity centre on the horizontal plane for the different Reynolds numbers. For $Re = 80$, after the initial transient (shown in dashed line), the gravity centre seems to rotate about an axis which tends to be at a fixed position. For $Re = 160$ and 240 the trajectories shown in figure 9a seems to suggest that for these Reynolds numbers the axis of rotation does not tend to a fixed position. This is reminiscent of the different regimes of sedimentation observed for simpler bodies, like spheres, disks and spheroids (Ern *et al.*, 2012).

To better understand the motion described by the seed in figure 9a, we compute the *moving axoid*, which is the locus of the instantaneous axis of rotation seen from a body fixed reference frame (Beju *et al.*, 1983). Note that the instantaneous axis of rotation is always parallel to $\mathbf{\Omega}$, which in turn is parallel to $\mathbf{k}_L$ (except for small deviations, as previously commented). Therefore, the *moving axoid* is a ruled surface which can be characterized by its intersection with the plane $z_L = z_R = 0$.

Figure 9b-d depicts the intersection of the *moving axoid* with the plane $z_R = 0$ for the different Re in Σ_R centered at G. For $Re = 80$ the intersection is a point (figure 9b), meanwhile for $Re = 160$ and 240 it is a circle (figure 9c and 9d). This indicates that for $Re = 80$ the seed gravity centre is rotating about a fixed axis in the laboratory reference frame, as we anticipated from figure 9a. On the other hand, the *moving axoid* for $Re = 240$ and 160 resembles that of a cylinder with its mass centre at a position different from its geometric centre, rolling without slipping over a surface. The radius of the intersection corresponds to the radius of the cylinder, and the distance from the centre of the intersection to G is the offset between the gravity centre and the geometric centre of the cylinder.

Therefore, the moving axoids shown in figure 9c and 9d are consistent with a seed rotating about an axis (the geometric centre of the intersection) which in turn is displacing, as we hypothesized from figure 9a. In this fashion, we can define $\mathbf{r}_{GR}$ to be the vector from G to the mean position of the intersection during the last four periods (represented with the symbol $\times$ in figure 9b-d). It is interesting to note that the modulus of $\mathbf{r}_{GR}$ decreases with Re (see table 1), while the angle between $\mathbf{r}_{GR}$ and $\mathbf{j}_R$,

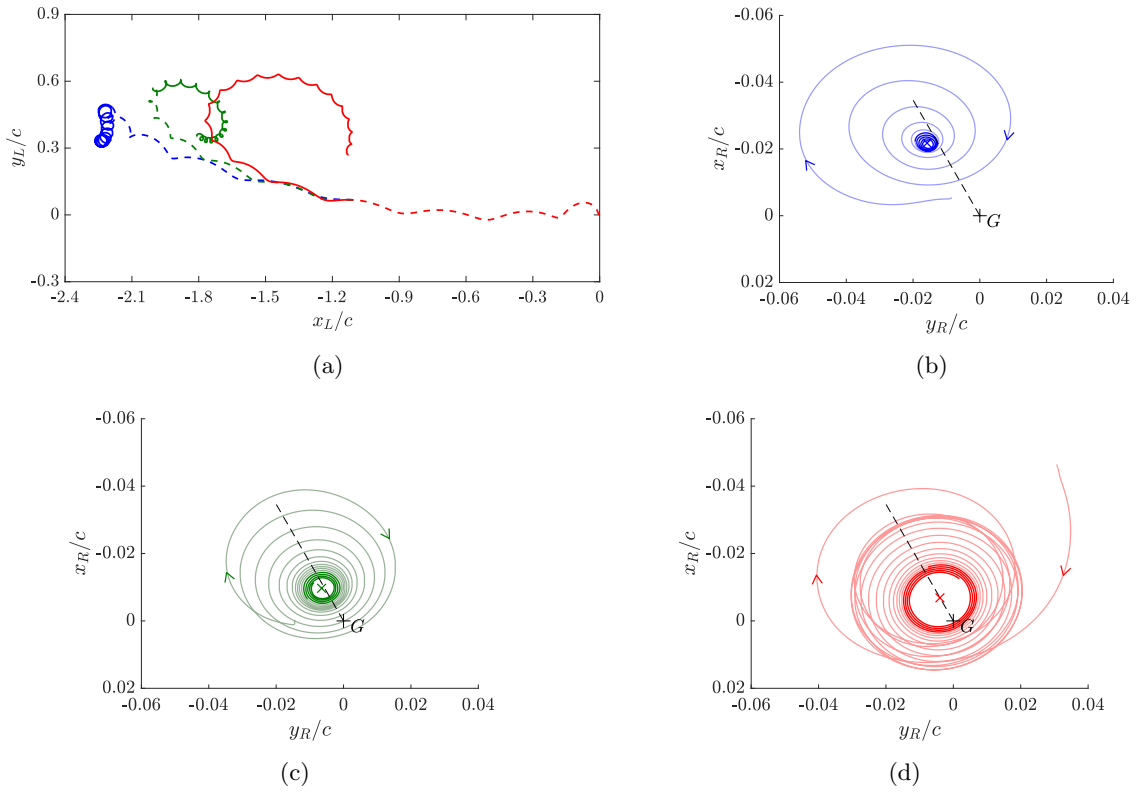

Figure 9: (a) Trajectory of the gravity centre, G on the horizontal plane. Line style: (−−) Resolution $256 \times 256 \times 256$ grid points, (——) resolution $512 \times 512 \times 512$ grid points. (——) $Re = 80$, (——) $Re = 160$ and (——) $Re = 240$. (b) (c) and (d) Intersection of the *moving axoid* with the horizontal plane $z_L/c = 0$. (b) $Re = 80$, (c) $Re = 160$, and (d) $Re = 240$. The intersection during the last four periods is highlighted. (×) is the mean position of the rotation axis averaged over the last four periods. The dashed line makes 120° with respect to y_c

	Forces			Moments		
Re	$\langle \tilde{F}_x^R \rangle$	$\langle \tilde{F}_y^R \rangle$	$\langle \tilde{F}_z^R \rangle$	$\langle \tilde{M}_x^R \rangle$	$\langle \tilde{M}_y^R \rangle$	$\langle \tilde{M}_z^R \rangle$
80	-0.46	-0.34	1.72	1.02	-0.25	$7 \cdot 10^{-4}$
160	-0.46	-0.30	2.48	1.70	-0.39	$7 \cdot 10^{-4}$
240	-0.43	-0.27	2.87	2.08	-0.46	$6 \cdot 10^{-4}$

Table 2: Average values of the forces and moments as a function of Re.

γ, remains constant for all Re and close to 120° (particularly it ranges from 126.0° for $Re = 80$, to 120.1° for $Re = 240$). This means that the seed is rotating while skidding (i.e, oversteering), which in the helicopter nomenclature corresponds to a positive lead angle equal to $\pi - \gamma$. Nevertheless, it should be stressed that as shown in table 1, $\tilde{r}_{GR} \sim 0.01$. Hence, the seed is rotating about a vertical axis which practically coincides with G, as we anticipated from the visualization of figure 4.

In sight of the above, we could attempt to split $\mathbf{u}_G$ into a rotational component, $\mathbf{u}_{G,r}$, and a displacement component, $\mathbf{u}_{G,d}$. The former would be the velocity of G relative to the rotation axis, that is $\mathbf{u}_G$ if the axis of rotation is fixed. Hence, the latter would be the velocity at which the axis of rotation *moves*. To calculate $\mathbf{u}_{G,d}$ we apply a low pass filter to $\mathbf{u}_G$, removing the frequencies greater than 1/2 the rotation frequency, $\Omega/2\pi$. The filtered signal corresponds to $\mathbf{u}_{G,d}$. Then, we calculate the modulus of $\mathbf{u}_{G,d}$, yielding $u_{G,d}/w_d = 0.0014$, 0.0058 and 0.0213 for $Re = 80, 160$ and 240, respectively. Therefore, as Re increases the seed rotates about a vertical axis which tends to move faster.

The displacement velocity, $\mathbf{u}_{G,d}$, may explain the increasing oscillations of β and θ with Re. The motion of the seed is analogous to the motion of a helicopter's blade in forward flight. The aerodynamic forces produced by the blade depend on the relative velocity of the fluid with respect to the blade. Higher velocities produce higher aerodynamic forces (Seddon and Newman, 2011). When the helicopter is fixed at a point, the relative velocity is radial and depends only on the angular velocity of the blade and the radial distance. In this fashion, the aerodynamic forces developed are constant throughout a cycle. However, when the helicopter is moving forward at a given velocity, $\mathbf{U}$ (or the flow surrounding it has a velocity $-\mathbf{U}$), the relative velocity of the blade depends also on its orientation with respect to the direction of the motion. Therefore, the aerodynamic forces would change depending on the azimuthal position of the blade.

For the case of the winged-seed, when it is moving with a velocity $\mathbf{u}_{G,d}$, a similar behaviour might be expected, with the addition that the seed is free to change its attitude. Hence, variations of the attitude could be expected due to the variation of the aerodynamic forces. In fact, the amplitude of the oscillations of the angles are in accordance to the amplitudes imposed to the helicopter's blades for the given advance ratios, $u_{G,d}/\Omega b$ (Seddon and Newman, 2011).

3.2 Dynamics and force equilibrium

After the analysis of the kinematics of motion, we proceed with the analysis of the aerodynamic forces. Table 2 gathers the mean aerodynamic forces and moments about G averaged over the last four periods and expressed in Σ_R. The forces are non-dimensionalized with $\rho_f w_d^2 c^2$ and the moments are non-dimensionalized with $\rho_f w_d^2 c^3$, such that $\tilde{F} = F/\rho_f w_d^2 c^2$ and $\tilde{M} = M/\rho_f w_d^2 c^3$.

The data in table 2 show that the horizontal forces ($\langle \tilde{F}_x^R \rangle$ and $\langle \tilde{F}_y^R \rangle$) slightly decrease in magnitude with Re, whereas the vertical force $\langle \tilde{F}_z^R \rangle$ substantially increases. The latter means that the *allowed* weight of a given seed increases with Re. On the other hand, if G is rotating about a vertical axis, the projection of the aerodynamic forces onto the horizontal plane should counteract the centrifugal force, i.e. it should be $m_s \Omega^2 \mathbf{r}_{GR}$. Indeed, the modulus of the horizontal component of $\tilde{\mathbf{F}}$ is 0.57, 0.55 and 0.51 for $Re = 80, 160$ and 240, respectively. These values are within a 2% of the average non-dimensional centrifugal force, namely $m_s \langle \tilde{\Omega} \rangle^2 \langle \tilde{r}_{GR} \rangle / \rho_f c^3$. It is also interesting to remark that even though r_{GR} is small, and one could presume the seed is rotating about G, this small distance is responsible for the slight decrease of $m_s \langle \tilde{\Omega} \rangle^2 \langle \tilde{r}_{GR} \rangle / \rho_f c^3$ with Re (i.e., Ω increases with Re). Moreover, the centrifugal force is of the same order as the vertical force. Finally, as expected, the resultant aerodynamic force points towards the axis of rotation and the angle between the horizontal projection of $\mathbf{F}$ and the y_c axis ranges from 126.1° for $Re = 80$, to 122.4° for $Re = 240$, in agreement with the position of the *moving axoids* in figure 9.

The moments along x_R and y_R are higher for higher Re. Note that this trend is in accordance with the behaviour of the forces, i.e.: higher vertical force and relatively constant horizontal forces. Note also

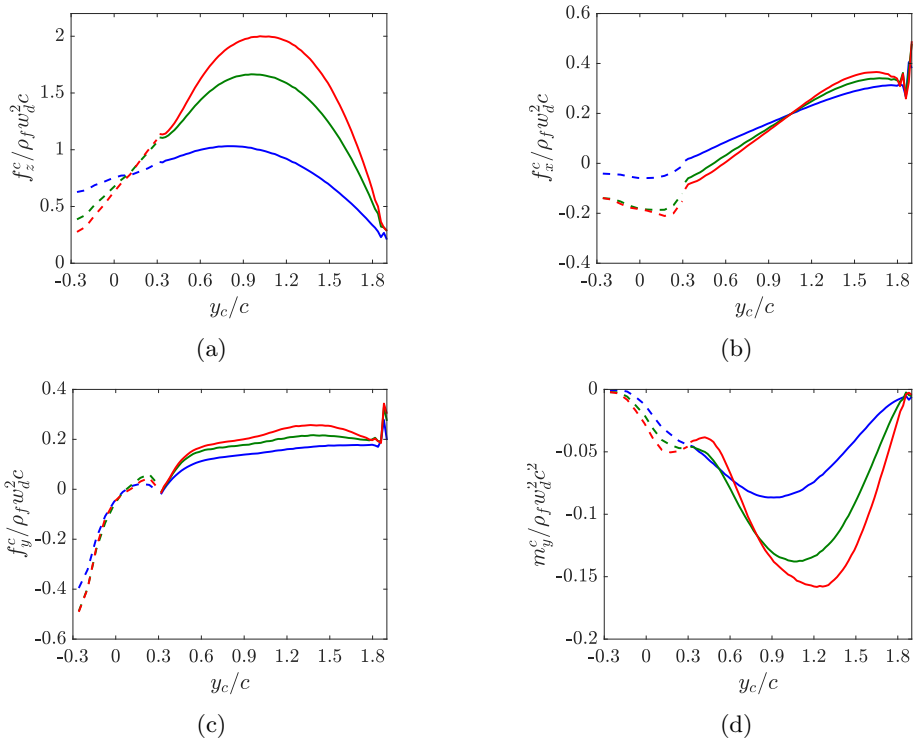

Figure 10: Forces and moment distribution over the seed in Σ_c reference frame for (——) $Re = 80$, (——) $Re = 160$ and (——) $Re = 240$. (a) Force distribution normal to the wing, f_z^c. (b) Force distribution tangential to the chordwise direction, $\mathbf{i}_c$, f_x^c. (c) Force distribution tangential to the spanwise direction, $\mathbf{j}_c$, f_y^c. (d) Pitching moment –i.e. moment along y_c axis–, m_y^c. Dashed lines correspond to the nut, continuous lines correspond to the wing.

that the latter is necessary to compensate the acceleration terms due to the rotation of the seed around an axis which is not parallel to a principal axis of inertia. On the other hand, the moment along z_R axis is nearly zero for all Re. This is a necessary consequence of having a constant angular velocity pointing along $\mathbf{k}_R$.

With the aim of explaining the previous trends, we analyse the force distribution on the seed with respect to Σ_c. We choose Σ_c because it is a body fixed reference frame whose vertical axis, z_c, is normal to the wing, which is the direction along which the aerodynamic force is largest.

Figure 10 shows the distribution of the three components of the aerodynamic force and the pitching moment with respect to the axis y_c (figure 10d). These quantities are non-dimensionalized using the descent speed, w_d, the chord, c, and the fluid density, ρ_f. The distributions are averaged over a time interval that corresponds to the last revolution of the seed. Note that the discretization of the wing is such that near the wing tip there are only a few lagrangian points per chord (see figure 3b), which leads to oscillations of the force distribution at this region.

As expected figure 10a shows that the largest contribution to F_z^c is produced by the wing. The contribution of the nut is also positive and it is likely more related to the drag experienced by the nut in a free-stream of velocity w_d, than to the fact that the seed is rotating. On the wing, the normal force distribution is roughly parabolic, with a peak value that increases and displaces towards the tip as Re increases. As a result, the integral of the normal force along the span increases as Re rises. This increase is likely a consequence of the larger angular velocity, yielding higher relative velocities.

On the contrary, the contribution of the force along the x_c direction, figure 10b, is very similar despite the different Ω among cases. In fact, the integral of F_x^c decreases with Re. This behaviour might be explained by the fact that these forces are associated to the skin friction (at least on the wing), rather than to the angular velocity. The nut and the sections of the wing closer to the nut are actually producing negative drag. Note that this region is close to the axis of rotation, and the flow pattern near the nut is complex (see figure 5). Therefore, the behaviour of the forces in this region cannot be easily explained.

The force distribution in the spanwise direction is shown in figure 10c. It is positive along the

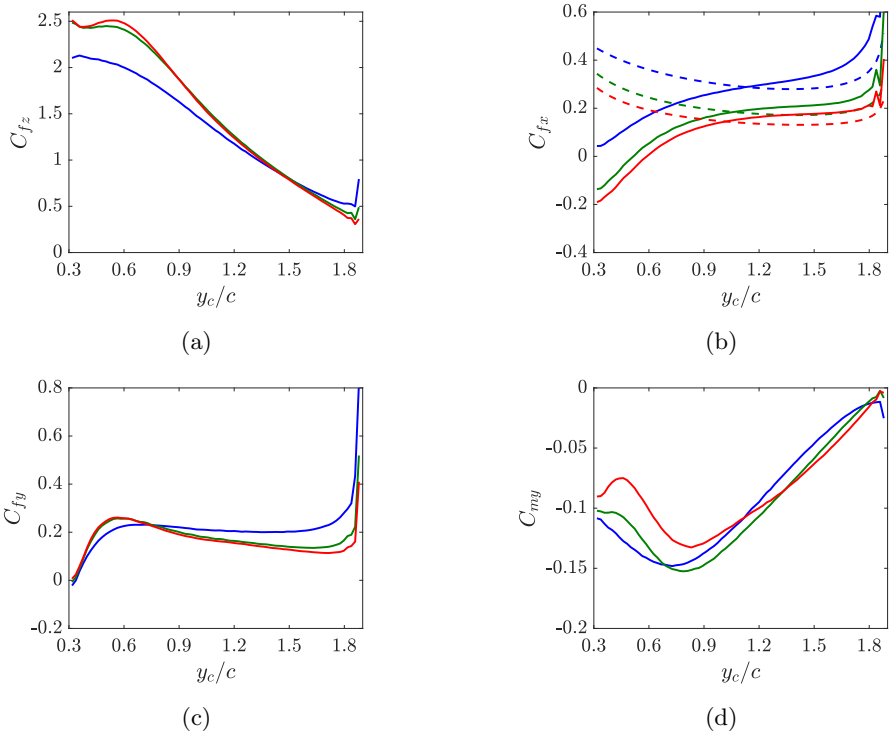

Figure 11: Forces and moment coefficients distribution over the seed in Σ_c reference frame for (——) $Re = 80$, (——) $Re = 160$ and (——) $Re = 240$. (a) Normal force coefficient, C_{fz}. (b) Tangential force coefficient, C_{fx}. Dashed lines are the friction coefficient calculated with the local chord $c(y_c)$ and the effective velocity $U_e(y_c)$. (c) Spanwise force coefficient C_{fy}. (d) Pitching moment coefficient C_{my}.

wing and relatively constant (slightly increasing with Re) meanwhile it becomes negative at the nut at $y_c \approx 0.15c$. Similarly to f_x^c, f_y^c is a tangential force, thus it is likely linked to skin friction rather than to pressure forces, as f_z^c. Hence, a positive spanwise force suggests the presence of a spanwise flow towards the tip, a hypothesis that is confirmed in Arranz *et al.* (2018).

The distribution of the pitching moment (figure 10d) along the span gives an indication of how the normal force is distributed along the chord at each spanwise section. Positive pitching moment means *nose up* moment about the y_c axis. For all Re the pitching moment is negative at every spanwise location. Therefore, there is a *nose down* moment about y_c for all Re along the span, which is consistent with $\langle \tilde{M}_y^R \rangle$. Note that the behaviour of the pitching moment with Re is similar to the one observed for f_z^c. This could be anticipated beforehand since the pitching is directly proportional to f_z^c.

The selection of the descent speed for the non-dimensionalization of the force in figure 10 is somewhat arbitrary. It could be argued that since the angular velocity changes with Re, this quantity should also enter in the non-dimensionalization of the aerodynamic forces. This idea is explored by defining the aerodynamic force and moment coefficients

$$C_f(y_c) = \frac{f^c}{\frac{1}{2}\rho_f U_e^2(y_c) c(y_c)}, \qquad C_m(y_c) = \frac{m^c}{\frac{1}{2}\rho_f U_e^2(y_c) c(y_c) c},$$

in terms of the modulus of the effective velocity at each wing section, $U_e(y_c) = \|\mathbf{u}_e(y_c)\|$, and the local chord, $c(y_c)$. Note that the effective velocity is a function of the descent speed, coning angle and angular velocity.

Figure 11 shows these aerodynamic force and moment coefficients along the span. Note that only the portion of the span corresponding to the wing is depicted in the figure since U_e has not been defined for the nut. In general, the force and moment coefficients tend to collapse better than in figure 10 (except possibly for C_{fx}), especially when only $Re = 160$ and 240 are considered. In figure 11a and figure 11d one can appreciate that C_{fz} and C_{my} tend to collapse for all Re for $y_c \geq 1.2c$. Thus, as we anticipated, f_z^c (and in turn, m_y^c) is highly linked to the relative velocity at each spanwise section, rather than to the Re. In other words, f_z^c is more related to pressure forces than to viscous forces. It is also noteworthy that C_{fz} along the span resembles the angle of attack distribution of figure 8b.

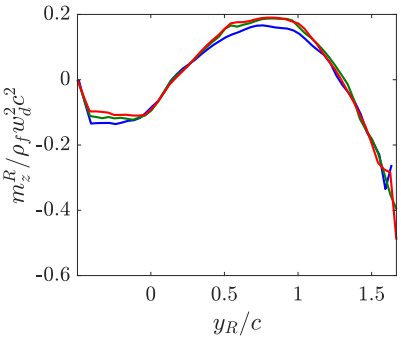

Figure 12: Vertical moment distribution, m_z^R along y_R direction. (——) $Re = 80$, (——) $Re = 160$ and (——) $Re = 240$.

As mentioned above, C_{fx} (figure 11b) seems to show a Re number dependency, decreasing as Re increases at any spanwise section. This behaviour is in agreement with the evolution of the skin friction coefficient of a flat plate with Re, which is included in figure figure 11b with dashed lines. Although the behaviour of the local friction coefficient is not the same as C_{fx} (in the calculation of the friction coefficient, it is assumed that the flow is aligned with the chord and three dimensional effects are not considered), it is observed that the offset among different Re coincides for both coefficients. Finally, the behaviour of C_{fy} (figure 11c) is more intricate, and it is probably linked to both viscous effects and centrifugal forces.

Integration of the previous forces yields $\mathbf{F}^R$. However, it is not clear *a priori* how these force distributions yield $\langle \tilde{M}_z^R \rangle \approx 0$. There are two possibilities: the distribution of the vertical moment is negligible at all spanwise sections (i.e., $m_z^R(y_R) \approx 0$ for all y_R), or the distribution is non-zero but it changes sign along y_R. Figure 12 depicts m_z^R as a function of y_R for the different Reynolds numbers, non-dimensionalized with the descent speed, w_d, the characteristic chord of the wing, c, and the fluid density ρ_f. Two facts are remarkable. First, the moment distribution is very similar for all Re despite the difference in the force distribution for the different cases. Second, the moment is negative near the nut and near the tip and positive elsewhere, which is very similar to the distribution of m_z^R in the blades of helicopters in auto-rotation (Cuerva *et al.*, 2009). Moreover, the spanwise section of *proper* auto-rotation (i.e. the spanwise section near the tip where $m_z^R = 0$) is at approximately 70% of the total span of the seed's wing, which is the characteristic spanwise section of auto-rotation of helicopter's blades (Cuerva *et al.*, 2006).

4 Conclusions

We present simulations of the auto-rotation of a model winged seed at various Reynolds numbers in the range $80 - 240$, keeping the seed's geometry and inertia constant. The calculations have been performed by solving the Navier-Stokes equations for the flow surrounding the seed using an immersed boundary method, together with the Newton-Euler rigid-body equations for the motion of the seed. Within this Reynolds number range, the seed attains a stable auto-rotative state, with an approximately constant angular velocity about a vertical axis. The coning angle and the pitch angle present small oscillations about a mean value for all Re under study. Both the mean value and the amplitude of the oscillations decrease as the Reynolds number is increased. Thus, with increasing Re, the seed tends to rotate at higher speeds, with less inclination with respect to the horizontal plane. The kinematics of the seed is similar to that reported in the literature in experiments with real winged seeds.

Also with increasing Re, it has been found that the translation of seed on the horizontal plane seems to increase. By computing the *moving axoid* we have observed that the vertical axis of rotation displaces, while the distance from the gravity centre of the seed to the axis remains rather constant for a given Re. Therefore, the lateral motion of the seed can be described as a regular rotation with respect to an axis which is drifting. This drifting velocity seems to increase with Re, and seems to be connected to the oscillations in β and θ. Moreover, we have found that the seed rotates while skidding (oversteering), resulting in an angle between the spanwise axis of the seed and the centrifugal forces (pointing towards the center of the moving axoid) of about $\gamma \approx 120°$, irrespective of the Re. In the helicopter nomenclature, this corresponds to a positive lead angle of the blade.

Points/c	$\tilde{F}_z$	ε_z	$\tilde{F}_x$	ε_x
32	1.8989	5.2%	0.9421	2.3%
40	1.8592	2.9%	0.9326	1.3%
48	1.8342	1.6%	0.9263	0.6%
64	1.8060	–	0.9205	–

Table 3: Non-dimensional forces and relative errors, ε, as a function of the resolution.

We have analysed the aerodynamic forces and moments acting on the seed. Is is observed that, with increasing Reynolds number, the horizontal components decrease in magnitude while the vertical component increases. Thus, the allowed weight of a given seed increases with the Reynolds number. Despite the displacement of the seed on the horizontal plane, and the oscillations of the angles (which lead to small variations in the angular velocity), a simplified equilibrium of forces and moments was found. The horizontal force is directed towards the axis of rotation and with a magnitude roughly equal to the centrifugal force. The moment about the vertical direction vanishes (as expected if the seed rotates with constant angular velocity about a vertical axis). In this regard, we have analysed the vertical moment distribution along the span that results in a zero moment. It has been found that it is very similar to typical moment distributions on auto-rotating helicopter blades, and it seems to be independent of Re.

The force distribution along the wing span was characterized using both global and local characteristic speeds and chord lengths for the non dimensionalisation of the force coefficients. It was found that the vertical component does not depend on the Reynolds number when using local scaling, suggesting that this component is mainly due to pressure force. On the other hand, the components tangent to the wing do present variations with the Reynolds number, so that they seem to be related to viscous forces.

Acknowledgements

This work was supported by grants TRA2013-41103-P (Mineco/Feder UE) and DPI2016-76151-C2-2-R (AEI/Feder UE). MGV was partially supported by a grant of the BBVA Foundation. The code was partially developed during a stay of MM (funded by BBVA) and MGV (funded by the Spanish Ministry of Education through the program José Castillejo) at the Karlsruhe Institute of Technology. The simulations were partially performed at the Steinbuch Centre for Computing (SCC), Karlsruhe. The computer resources, technical expertise and assistance provided by this center are thankfully acknowledged.

A Grid refinement study

A grid refinement study was performed to determine the grid resolution to be employed in the simulations. The study was performed by externally imposing the attitude and angular velocity of the seed. The attitude of the seed and angular velocity were chosen corresponding to those obtained in a preliminary calculation of the auto-rotating seed at $Re = 75$ with high resolution. Therefore, the imposed motion of the seed is defined by $\langle\beta\rangle = 15.91°$, $\langle\theta\rangle = -25.48°$ and $\langle\tilde{\Omega}\rangle = 0.89$. We then performed several simulations varying the grid resolution at $Re = 240$, to study the convergence of the aerodynamic forces. These simulations were performed in a computational domain of dimensions $x_L/c \in [-2, 2]$, $y_L/c \in [-2, 2]$ and $z_L/c \in [-3, 5]$, with *free-slip* boundary conditions at the lateral walls, an inflow at the bottom wall and advective boundary condition at the top wall. Note that *free-slip* boundary conditions are imposed at the lateral walls because the gravity centre of the seed is fixed at the center of the horizontal plane $z_L = 0$. Therefore, the seed cannot cross the lateral boundaries, as it may occur when the seed is free to move on the horizontal plane.

Four grid resolutions were tested, 32, 40, 48 and 64 points per chord length, which correspond to domains of $128 \times 128 \times 256$ grid points, $160 \times 160 \times 320$ grid points, $256 \times 256 \times 512$ grid points, and $512 \times 512 \times 768$ grid points, respectively.

The variation of the vertical (F_z) and horizontal (F_x) aerodynamic forces non-dimensionalized with $\rho_f w_d^2 c^2$, as well as their relative error, ε, are gathered in table 3. The relative error is calculated using the forces obtained with 64 points/c, averaged over one period, as reference values:

$$\varepsilon_{z,x} = \frac{|\tilde{F}_{z,x} - \tilde{F}^{64}_{z,x}|}{\tilde{F}^{64}_{z,x}} \tag{12}$$

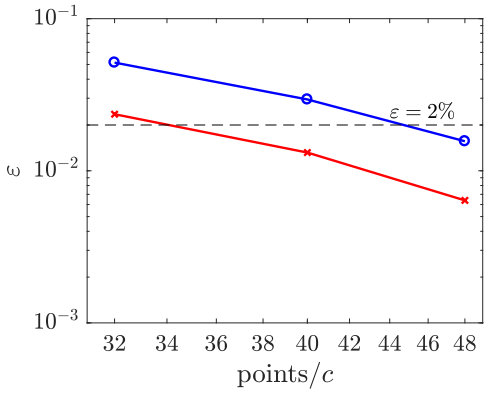

Figure 13: Variation of the relative error of the vertical force, (—o—) ε_z, and the horizontal force, (—×—) ε_x, with the resolution.

Figure 13 displays the variation of ε_z and ε_x with the resolution. There, one can appreciate that for resolutions higher than 32 points/c, ε_x is less than 2%. Likewise, for 48 points/c, ε_z is also less than 2%. Therefore, we choose a resolution of 48 points/c since both ε_x and ε_z are smaller than 2%. Although the grid refinement study was performed for $Re = 240$, the same grid was employed for the cases $Re = 80$ and $Re = 160$, for which the results are expected to be correspondingly more accurate.

References

Arranz, G., Gonzalo, A., Uhlmann, M., Flores, O., and García-Villalba, M. A numerical study of the flow around a model winged seed in auto-rotation. 2018. Submitted to *Flow Turbul. Combust.*

Azuma, A. *The biokinetics of flying and swimming.* Springer-Verlag, 1992. doi:10.1007/978-4-431-68210-3.

Azuma, A. and Yasuda, K. Flight performance of rotary seeds. *J. Theor. Biol.*, **138**(1):23–53, 1989. doi:10.1016/S0022-5193(89)80176-6.

Beju, I., Soós, E., and Teodorescu, P. *Euclidean tensor calculus with applications.* CRC Press, 1983.

Burrows, F. M. Wind-borne seed and fruit movement. *New Phytol.*, **75**(2):405–418, 1975. doi:10.1111/j.1469-8137.1975.tb01404.x.

Chrust, M. *Etude numérique de la chute libre d'objets axisymétriques dans un fluide newtonien.* Ph.D. thesis, Strasbourg, 2012.

Cuerva, A., Espino, J. L., López, O., Meseguer, J., and Sanz, A. *Teoría de los helicópteros.* Madrid: ETSI Aeronáuticos, UPM, 2009.

Cuerva, A., Sanz-Andrés, A., Meseguer, J., and Espino, J. L. An engineering modification of the blade element momentum equation for vertical descent: an autoration case study. *J. Am. Helicopter Soc.*, **51**(4):341–348, 2006. doi:10.4050/JAHS.51.341.

Ern, P., Risso, F., Fabre, D., and Magnaudet, J. Wake-induced oscillatory paths of bodies freely rising or falling in fluids. *Annu. Rev. Fluid Mech.*, **44**:97–121, 2012. doi:10.1146/annurev-fluid-120710-101250.

Fregene, K. and Bolden, C. L. Dynamics and control of a biomimetic single-wing nano air vehicle. In *American Control Conference (ACC), 2010*, pages 51–56. IEEE, 2010. doi:10.1109/ACC.2010.5531206.

Green, D. S. The terminal velocity and dispersal of spinning samaras. *Am. J. Bot.*, **67**(8):1218–1224, 1980. doi:10.1002/j.1537-2197.1980.tb07754.x.

Hunt, J. C. R., Wray, A. A., and Moin, P. Eddies, stream, and convergence zones in turbulent flows. **Report CTR-S88**, 1988.

Lee, I. and Choi, H. Flight of a falling maple seed. *Phys. Rev. Fluids*, **2**:090511, 2017. doi:10.1103/PhysRevFluids.2.090511.

Lentink, D., Dickson, W. B., van Leeuwen, J. L., and Dickinson, M. H. Leading-edge vortices elevate lift of autorotating plant seeds. *Science*, **324**(5933):1438–1440, 2009. doi:10.1126/science.1174196.

Limacher, E. and Rival, D. E. On the distribution of leading-edge vortex circulation in samara-like flight. *J. Fluid Mech.*, **776**:316–333, 2015. doi:10.1017/jfm.2015.279.

Miller, A., Muljadi, E., and Zinger, D. S. A variable speed wind turbine power control. *IEEE T. Energy Conver.*, **12**(2):181–186, 1997. doi:10.1109/60.629701.

Minami, S. and Azuma, A. Various flying modes of wind-dispersal seeds. *J. Theor. Biol.*, **225**(1):1–14, 2003. doi:10.1016/S0022-5193(03)00216-9.

Moriche, M. *A numerical study on the aerodynamic forces and the wake stability of flapping flight at low Reynolds number*. Ph.D. thesis, Univ. Carlos III Madrid, 2017.

Moriche, M., Flores, O., and García-Villalba, M. Three-dimensional instabilities in the wake of a flapping wing at low Reynolds number. *Int. J. Heat Fluid Flow*, **62A**:44–55, 2016. doi:10.1016/j.ijheatfluidflow.2016.06.015.

Moriche, M., Flores, O., and García-Villalba, M. On the aerodynamic forces on heaving and pitching airfoils at low Reynolds number. *J. Fluid Mech.*, **828**:395–423, 2017. doi:10.1017/jfm.2017.508.

Nathan, R. Long-distance dispersal of plants. *Science*, **313**(5788):786–788, 2006. doi:10.1126/science.1124975.

Norberg, R. Autorotation, self-stability, and structure of single-winged fruits and seeds (samaras) with comparative remarks on animal flight. *Biol. Rev.*, **48**(4):561–596, 1973. doi:10.1111/j.1469-185X.1973.tb01569.x.

Obradovic, B., Ho, G., Barto, R., Fregene, K., and Sharp, D. A multi-scale simulation methodology for the samarai monocopter μUAV. In *AIAA Modeling and Simulation Technologies Conference*, page 5012. 2012. doi:10.2514/6.2012-5012.

Ortega-Jiménez, V. M., Martín-Alcántara, A., Fernández-Feria, R., and Dudley, R. On the autorotation of animal wings. *J. R. Soc. Interface*, **14**(126):20160870, 2017. doi:10.1098/rsif.2016.0870.

Pedersen, C. B. and Żbikowski, R. *An indicial-Polhamus aerodynamic model of insect-like flapping wings in hover*, volume 2 of *Flow Phenomena in Nature*, pages 606–666. Liebe, R., 2006.

Pounds, P. and Singh, S. Samara: Biologically inspired self-deploying sensor networks. *IEEE Potentials*, **34**(2):10–14, 2015. doi:10.1109/MPOT.2014.2359034.

Rosen, A. and Seter, D. Vertical autorotation of a single-winged samara. *J. App. Mech.*, **58**(4):1064–1071, 1991. doi:10.1115/1.2897683.

Salcedo, E., Treviño, C., Vargas, R. O., and Martínez-Suástegui, L. Stereoscopic particle image velocimetry measurements of the three-dimensional flow field of a descending autorotating mahogany seed (*Swietenia macrophylla*). *J. Exp. Biol.*, **216**(11):2017–2030, 2013. doi:10.1242/jeb.085407.

Seddon, J. M. and Newman, S. *Basic helicopter aerodynamics*. Wiley, Chichester, West Sussex, UK, 3rd edition, 2011.

Seter, D. and Rosen, A. Stability of the vertical autorotation of a single-winged samara. *J. App. Mech.*, **59**(4):1000–1008, 1992a. doi:10.1115/1.2894014.

Seter, D. and Rosen, A. Study of the vertical autorotation of a single-winged samara. *Biol. Rev.*, **67**(2):175–197, 1992b. doi:10.1111/j.1469-185X.1992.tb01018.x.

Tewari, A. *Atmospheric and space flight dynamics*. Springer, 2007.

Uhlmann, M. An immersed boundary method with direct forcing for the simulation of particulate flows. *J. Comput. Phys.*, **209**(2):448–476, 2005. doi:10.1016/j.jcp.2005.03.017.

Uhlmann, M. and Dušek, J. The motion of a single heavy sphere in ambient fluid: A benchmark for interface-resolved particulate flow simulations with significant relative velocities. *Int. J. Multiphas. Flow*, **59**:221 – 243, 2014. doi:10.1016/j.ijmultiphaseflow.2013.10.010.

Ulrich, E. and Pines, D. J. Effects of planform geometry on mechanical samara autorotation efficiency and rotational dynamics. *J. Am. Helicopter Soc.*, **57**(1):1–10, 2012. doi:10.4050/JAHS.57.012003.

Ulrich, E. R., Darryll, P., and Humbert, J. S. From falling to flying: the path to powered flight of a robotic samara nano air vehicle. *Bioinspir. Biomim.*, **5**(4):045009, 2010. doi:10.1088/1748-3182/5/4/045009.

Varshney, K., Chang, S., and Wang, Z. J. The kinematics of falling maple seeds and the initial transition to a helical motion. *Nonlinearity*, **25**(1):C1, 2012. doi:10.1088/0951-7715/25/1/C1.

Yasuda, K. and Azuma, A. The autorotation boundary in the flight of samaras. *J. Theor. Biol.*, **185**(3):313–320, 1997. doi:10.1006/jtbi.1996.0299.